

FERMI BUBBLES: EVIDENCE FOR A POSSIBLE RECENT AGN JET ACTIVITY IN THE GALAXY

FULAI GUO¹ AND WILLIAM G. MATHEWS¹

Draft version December 2, 2024

ABSTRACT

The *Fermi Gamma-ray Space Telescope* reveals two large gamma-ray bubbles in the Galaxy, which extend about 50° (~ 10 kpc) above and below the Galactic center and are symmetric about the Galactic plane. Using axisymmetric hydrodynamic simulations with a self-consistent treatment of the dynamical cosmic ray (CR) - gas interaction, we show that the bubbles can be created with a recent AGN jet activity about 1 - 2 Myr ago, which was active for a duration of $\sim 0.1 - 0.5$ Myr, releasing a total energy of $\sim 1 - 8 \times 10^{57}$ erg. The bipolar jets were ejected into the Galactic halo along the symmetric axis perpendicular to the Galactic plane. Near the Galactic center, the jets must be moderately light with a typical density contrast $0.001 \lesssim \eta \lesssim 0.1$ relative to the ambient hot gas. The jets are energetically dominated by kinetic energy, and over-pressured with CR pressure which induces lateral jet expansion, creating fat CR bubbles as observed. The sharp edges of the bubbles imply that CR diffusion across the bubble surface is strongly suppressed. The jet activity induces a strong shock, which heats and compresses the ambient gas in the Galactic halo, successfully explaining the *ROSAT* X-ray features surrounding the bubbles. Fermi bubbles provide strong evidence for a recent powerful AGN jet activity in our Galaxy, shedding new insights into the origin of the halo CR population and the detailed mechanism through which active galactic nucleus feedback regulates the co-evolution of massive black holes and their host bulges.

Subject headings: cosmic rays – galaxies: active – galaxies: jets – Galaxy: nucleus – gamma rays: galaxies

1. INTRODUCTION

Using 1.6 years of data from the *Fermi Gamma-ray Space Telescope*, Su et al. (2010) discovered two large gamma-ray bubbles emitting at $1 \lesssim E_\gamma \lesssim 50$ GeV in our Galaxy. They are denoted as the ‘Fermi bubbles’, and extend to $\sim 50^\circ$ above and below the Galactic center (GC), with a width of about 40° in longitude. They have approximately uniform surface brightness with sharp edges. The bubbles were previously identified as the ‘Fermi haze’ from the first year *Fermi* data (Dobler et al. 2010). The gamma-ray emission associated with the bubbles has a hard spectrum ($dN_\gamma/dE_\gamma \sim E_\gamma^{-2}$), and is most likely to originate from the inverse Compton (IC) scattering of cosmic ray (CR) electrons with the interstellar radiation field (ISRF; Dobler et al. 2010, Su et al. 2010). The hard CR electron (CRe) population also produces microwave synchrotron radiation, which was previously invoked to explain the microwave haze (at tens of GHz) discovered by the *Wilkinson Microwave Anisotropy Probe* (WMAP) - the ‘WMAP haze’, which is spatially associated with the Fermi bubbles (Finkbeiner 2004; Dobler & Finkbeiner 2008).

The bilobular morphology of the Fermi bubbles suggests that the responsible CRe population is not made of diffused electrons originally accelerated by supernova (SN) shocks in the Galactic plane, which also tend to have a much softer spectrum as CRes preferentially lose energy at high energies during the diffusion. Furthermore, the sharp edges of the Fermi bubbles imply that the diffusion is strongly suppressed across the bubble sur-

face (see Section 3.2). Similarly, the morphology and sharp edges of the Fermi bubbles indicate that the CRes in the Fermi bubbles are not byproducts of dark matter annihilations.

As pointed out by Su et al. (2010), the Fermi bubbles were most likely created by some large episode of energy injection in the GC, e.g., jets originating from active galactic nucleus (AGN) activity or a nuclear starburst. However, the typical speed of galactic starburst winds is about 200-300 km s⁻¹, which is too slow to transport CRs, considering the short IC cooling time of CRes at tens of GeV in the ISRF. Furthermore, the shocks produced by the starburst may not be strong enough to efficiently accelerate CRs to tens of GeV. In contrast, relativistic or sub-relativistic AGN jets can accelerate and transport CRs very efficiently.

In this paper we use hydrodynamic simulations to perform a feasibility study, investigating if the main features of the Fermi bubbles can be reproduced by a recent AGN jet activity from the GC. Our calculations take into account the dynamical interactions between CRs and thermal gas, self-consistently modeling the CR advection with the thermal gas. Our two-dimensional (2D) calculations allow us to do a fast parameter study, identifying appropriate jet parameters. We show that to reproduce the morphology of Fermi bubbles, successful AGN jets cannot be either too massive or too light, but are constrained to have densities about 0.001 - 0.1 times the density of the initial ambient hot gas near the GC (i.e., with density contrasts $0.001 \lesssim \eta \lesssim 0.1$). In particular, the observed Fermi bubbles can be approximately reproduced by a pair of bipolar AGN jets which began about 1 - 2 Myr ago, and were active for a duration of $\sim 0.1 - 0.5$ Myr, each releasing a typical energy of $\sim 10^{57}$ erg. We

¹ UCO/Lick Observatory, Department of Astronomy and Astrophysics, University of California, Santa Cruz, CA 95064, USA; fulai@ucolick.org

also show that to produce the sharp outer edges of the bubbles seen in gamma ray emission, CR diffusion across the bubble boundaries must be strongly suppressed.

The detection of Fermi bubbles thus provides strong evidence for a recent powerful AGN event in our Galaxy, which suggests that AGN jets from the GC may contribute significantly to the halo CR population. Our opposing jet model for the Fermi bubbles is inspired by similar non-thermal double jet events observed in massive galaxies, particularly those lying at the centers of galaxy groups and clusters. The energy provided by central black holes is of essential importance in galaxy evolution. Observations indicate that black hole masses are tightly correlated with the stellar mass and the stellar velocity dispersion within their host galaxy bulges (e.g., Magorrian et al. 1998; Ferrarese & Merritt 2000; Gebhardt et al. 2000). AGN jets carry a large amount of energy and momentum, a fraction of which may be deposited within galactic bulges, significantly affecting the evolution of bulges and central massive black holes, and thus explaining the origin of their co-evolution. The detection of Fermi bubbles suggests that AGN jet feedback has been operating in our Galaxy, shaping the joint evolution of the Galactic bubble and its central black hole.

The rest of the paper is organized as follows. In Section 2, we describe CR transport in the Galaxy, our Galactic model, and numerical setup. We present our results in Section 3, and summarize our main conclusions with implications in Section 4.

2. THE MODEL AND NUMERICAL METHODS

2.1. Cosmic Ray Transport in the Galaxy

The observed Fermi bubbles are offset from the Galactic center with one above and the other below the Galactic plane. They extend to about 50° (~ 10 kpc) above and below the GC, and are symmetric about the Galactic plane. Here we assume that the distance from the Sun to the GC is $R_\odot = 8.5$ kpc. In *Fermi* maps, the bubbles are seen at $1 \lesssim E_\gamma \lesssim 50$ GeV, corresponding to relativistic CRs with energies $10 \lesssim E_{\text{cr}} \lesssim 100$ GeV if the observed γ rays are inverse Compton upscattering of starlight by these CRs. The IC cooling time of these CR electrons is typically a few million years, depending on their energies and locations (see Figure 28 of Su et al. 2010). Due to the short age and symmetry of these two bubbles, they probably share the same origin. It is unclear if any mechanism could accelerate or reaccelerate CRs at the same time in situ in these two bubbles separated by 10 kpc from each other. It is more likely that CRs in these two bubbles are produced by one single activity and transported to these two bubbles. If this scenario is correct, the location of CR production is likely the midpoint between the bubbles, the GC.

Each CR particle has a velocity near the speed of light. However, it is well known that the collective transport speed of CRs in the Galaxy is much smaller (e.g., the CRs reaching the Earth are observed to be highly isotropic). This is commonly explained by the scattering of CRs by magnetic irregularities. When the scattering is significant, CRs are strongly trapped and ‘effectively’ move with magnetic irregularities, which are frozen in the hot plasma. Therefore, CRs are advected with thermal gas at the local gas velocity, and in this case, the CR transport

is usually called advection. In regions where the magnetic field is locally aligned, CRs may stream through thermal gas, but the streaming speed is limited by the Alfvén speed. If CRs stream along the magnetic field lines at a speed faster than the local Alfvén speed, the CR streaming instability is triggered and excites Alfvén waves, which significantly scatter CRs in return (Skilling 1971; also see Kulsrud 2005, Chap. 12). Consequently, the CR streaming speed relative to the gas is roughly the local Alfvén speed. Due to the unknown and possibly complex magnetic field structure, CR streaming relative to the local gas is often ignored, as we assume in this paper. This is a good approximation in many cases, where CR scattering off magnetic irregularities is significant and/or the Alfvén speed is much smaller than the local gas speed.

In addition to advection, CRs can also diffuse through the thermal gas, as they scatter off magnetic inhomogeneities. CR diffusion is usually described by the CR diffusion coefficient κ , which probably depends on the magnetic field structure and CR energy. Typical values of κ in the Galaxy is found to be $\kappa \sim (3 - 5) \times 10^{28} \text{ cm}^2 \text{ s}^{-1}$ (Strong et al. 2007).

The Fermi bubbles extend up to ~ 10 kpc away from the GC. If the CRs in the bubbles are produced at the GC, they must be transported very quickly, at a speed of $v_{\text{transport}} \sim (c/30)(t_{\text{age}}/1 \text{ Myr})^{-1}$, to form the bubbles, where c is the speed of light and t_{age} is the age of the Fermi bubbles. t_{age} is less than a few million years due to the constraint from the short cooling times of CRs responsible for the detected γ -ray emission. Obviously, the main CR transport mechanism is not diffusion, which would form one single gamma-ray bubble centered at the GC and is too slow to transport CRs. To transport CRs for a distance of $l = 10$ kpc within t_{age} by diffusion, the required diffusion coefficient is $\kappa \sim l^2/t_{\text{age}} \sim 3 \times 10^{31}(t_{\text{age}}/1 \text{ Myr})^{-1} \text{ cm}^2 \text{ s}^{-1}$, three orders of magnitude larger than typical estimates of the CR diffusivity in the Galaxy. Furthermore, long diffusion times tend to soften the spectra of CRs and the resulting gamma-ray emission, while the observed gamma-ray spectrum from the bubbles is distinctly hard ($dN_\gamma/dE_\gamma \sim E_\gamma^{-2}$; even harder than expected IC emission of CRs accelerated in SN shocks in the Galactic disk) and is quite uniform through the bubbles (Su et al. 2010).

Since diffusion is not responsible for transporting CRs from the GC to the Fermi bubbles, advection with thermal gas is the only possible CR transport mechanism. Strong CR advection may be induced by galactic winds or AGN jets from the GC. The typical speed of galactic winds is about $200\text{-}300 \text{ km s}^{-1}$, which is more than one order of magnitude below $v_{\text{transport}}$, the required CR transport speed to form the Fermi bubbles. In other words, it takes about 50 Myr for galactic winds to reach 10 kpc, but there is no evidence of cooling losses in gamma-ray intensity and spectrum. On the other hand, extragalactic AGN jets typically have relativistic or near relativistic velocities, and, with their smaller cross-sectional areas, decelerate much slower than galactic winds. The propagation of AGN jets is determined by the speed of hotspots at the jet extremities, and may be close to $v_{\text{transport}}$, depending on both jet parameters

and the ambient gas properties. The primary goal of our paper is to study with numerical simulations the possibility of forming the Fermi bubbles with CR-carrying AGN jets from the GC.

The CR transport in the Galaxy has been studied numerically by some simulation codes, in particular, the Galactic Propagation (GALPROP) code (Strong & Moskalenko 1998), which is very detailed, including three-dimensional distributions of gas, dust, magnetic fields, optical and FIR photons. However, GALPROP is not able to self-consistently model CR advection, which is important when significant gas motions are present. In addition to jet motions, CR pressure gradients can also produce gas motions, which in return advect the CRs. Thus, dynamical interactions between CRs and the background gas should be taken into account to self-consistently model CR transport, particularly advection.

We have developed a finite-differencing code to numerically study CR transport and the dynamical interaction between CRs and hot gas, which has been successfully used to study X-ray cavities and radio bubbles in galaxy clusters in a series of papers, e.g., Mathews & Brighenti (2008a), Mathews & Brighenti (2008b), Mathews (2009), Guo & Mathews (2010a), Guo & Mathews (2010b), and Mathews & Guo (2010). More recently, we use our code to study the evolution of CR-dominated AGN jets in galaxy clusters in Guo & Mathews (2011). In this paper, we intend to modify our code to study AGN jets and the formation of Fermi bubbles in the Milky Way. In the rest of this section, we will elaborate the basic equations and assumptions of our model, and the setup of our numerical procedure.

2.2. Equations and Assumptions

The dynamical interaction between CRs and thermal gas may be described by the CR pressure P_c . In our calculations, we directly follow the temporal and spatial evolution of the CR energy density e_c , which is related to P_c through $P_c = (\gamma_c - 1)e_c$, where $\gamma_c = 4/3$. The nature of the relativistic particles with energy density e_c is unspecified and may be electrons and/or protons, although gamma-ray emission of the Fermi bubbles may be mainly produced by CR electrons. CR pressure gradients can accelerate thermal gas, converting CR energy into the kinetic energy of thermal gas, which may be further converted to the internal gas energy in shocks or other compressions. The combined hydrodynamic evolution of thermal gas and CRs can be described by the following four equations:

$$\frac{d\rho}{dt} + \rho \nabla \cdot \mathbf{v} = 0, \quad (1)$$

$$\rho \frac{d\mathbf{v}}{dt} = -\nabla(P + P_c) - \rho \nabla \Phi, \quad (2)$$

$$\frac{\partial e}{\partial t} + \nabla \cdot (e\mathbf{v}) = -P \nabla \cdot \mathbf{v}, \quad (3)$$

$$\frac{\partial e_c}{\partial t} + \nabla \cdot (e_c \mathbf{v}) = -P_c \nabla \cdot \mathbf{v} + \nabla \cdot (\kappa \nabla e_c), \quad (4)$$

where $d/dt \equiv \partial/\partial t + \mathbf{v} \cdot \nabla$ is the Lagrangian time derivative, κ is the CR diffusion coefficient, and all other variables have their usual meanings. The gas pressure P is related with the gas internal energy density e via $P = (\gamma - 1)e$, where we assume $\gamma = 5/3$.

The Galactic potential Φ is mainly contributed by three components: the bulge, disk and dark matter halo. We assume that it is fixed with time and neglect the small contribution from hot halo gas. We explain our simple Galactic potential model and initial conditions for the thermal gas in Section 2.3. We ignore radiative cooling of thermal gas, which is unimportant during the short-duration ($\lesssim 1\text{-}3$ Myr) of our simulations. The gas temperature is related to the gas pressure and density via the ideal gas law:

$$T = \frac{\mu m_\mu P}{k_B \rho}, \quad (5)$$

where k_B is Boltzmann's constant, m_μ is the atomic mass unit, and $\mu = 0.61$ is the molecular weight. To avoid confusion we denote the gas pressure P as P_g in the rest of the paper.

At time $t = 0$ we assume that the CR energy density is zero in the Galaxy, $e_c = 0$, but at later times CRs enter the Galactic halo in jets from the GC. Equation 4 describes the evolution of CR energy density including both advection and diffusion. The CR diffusion coefficient κ likely depends on the magnetic field structure and CR energy, but for simplicity, we assume that it is a constant in space and time: $\kappa \sim 3 \times 10^{27} - 3 \times 10^{29} \text{ cm}^2 \text{ s}^{-1}$ (see Table 1). We explore the effect of various diffusion coefficients on the formation of Fermi bubbles in Section 3.2, where we also consider a case with a spatially-varying diffusion coefficient.

As discussed in the previous subsection, CRs interact with magnetic irregularities and Alfvén waves, effectively exerting CR pressure gradients on the thermal gas (equation 2). Pressure gradients in the CR component act directly on the gas by means of magnetic fields frozen into the gas. This is the primary interaction between CRs and thermal gas. We neglect other more complicated (probably secondary) interactions, e.g., Coulomb interactions, hadronic collisions, and hydromagnetic-wave-mediated CR heating, that all depend on the CR energy spectrum (e.g., Guo & Oh 2008). Since the jet evolution in our calculation is mainly driven by its kinetic energy and the injected CR energy, the dynamical effect of magnetic fields is expected to be moderate and not significantly alter our results (see our estimates in Section 3.1). More sophisticated magnetohydrodynamical calculations are necessary in the future to explore the impact of magnetic fields. We also neglect CR energy losses from synchrotron and IC emissions. Observations by the Fermi telescope of Fermi bubbles do not show significant cooling in gamma-ray intensity and spectrum, and the integrated CR energy density e_c may be mainly contributed by low-energy CR electrons and possibly CR protons, which have much longer lifetimes than high-energy CR electrons.

2.3. The Galactic Model

Our key objective in this paper is to perform a feasibility study to determine if the Fermi bubbles can be

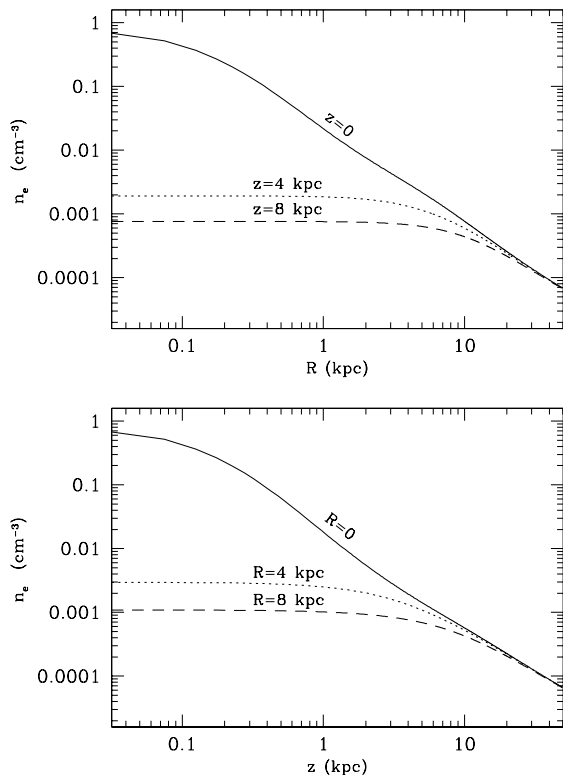


FIG. 1.— Initial profiles of electron number density of the hot gas in the Galactic halo along the R direction (parallel to the Galactic plane) at three fixed values of z (top panel) and along the z direction (perpendicular to the Galactic plane) at three fixed values of R (bottom panel). The density distribution $n_e(R, z)$ is solved from hydrostatic equilibrium, a spatially uniform temperature $T = 2.4 \times 10^6$ K, and a given value for the electron number density at the origin, $n_{e0} = 1 \text{ cm}^{-3}$.

created with jets from the GC that are apparently no longer active. The Fermi bubbles are inertially confined by pre-existing gas in the Galactic halo having temperatures of $\sim 10^6$ K. For simplicity, we assume that the hot gaseous halo is initially isothermal with temperature $T = 2.4 \times 10^6$ K, as inferred from X-ray absorption line studies (Yao & Wang 2005). To derive the initial density distribution of the hot gas, we further assume that the gas is initially in hydrostatic equilibrium. We adopt the Galactic potential from Helmi & White (2001), where the Galaxy is represented by a fixed potential with three components: a dark logarithmic halo

$$\Phi_{\text{halo}} = v_{\text{halo}}^2 \ln(r^2 + d_{\text{h}}^2), \quad (6)$$

a Miyamoto-Nagai disc

$$\Phi_{\text{disc}} = -\frac{GM_{\text{disc}}}{\sqrt{R^2 + (a + \sqrt{z^2 + b^2})^2}}, \quad (7)$$

and a spherical Hernquist stellar bulge

$$\Phi_{\text{bulge}} = -\frac{GM_{\text{bulge}}}{r + d_{\text{b}}}, \quad (8)$$

where R is the galactocentric radius in the Galactic plane, $r = \sqrt{R^2 + z^2}$ is the spatial distance to the GC, $v_{\text{halo}} = 131.5 \text{ km s}^{-1}$ and $d_{\text{h}} = 12 \text{ kpc}$; $M_{\text{disc}} = 10^{11} M_{\odot}$, $a = 6.5 \text{ kpc}$ and $b = 0.26 \text{ kpc}$; $M_{\text{bulge}} = 3.4 \times 10^{10} M_{\odot}$ and $d_{\text{b}} = 0.7 \text{ kpc}$. We have also explored alternative models

of the Galactic potential from Breitschwerdt et al. (1991) and Wolfire et al. (1995), and found that the resulting gas density distribution is similar.

For the hot gas, it is convenient to use the electron number density n_e , which is related to the gas density through

$$\rho = \mu_e n_e m_{\mu}, \quad (9)$$

where $\mu_e = 5\mu/(2 + \mu)$ is the molecular weight per electron. For a given value of electron number density at the origin n_{e0} , we derive the spatial distribution of n_e from hydrostatic equilibrium and the spatially-uniform temperature $T = 2.4 \times 10^6$ K. In the rest of this paper, we adopt the n_e distribution with $n_{e0} = 1 \text{ cm}^{-3}$, which gives electron number densities on the order of 10^{-3} cm^{-3} at galactocentric distances of a few kpc. Figure 1 shows the resulting n_e profiles along the R direction for three fixed values of z and along the z direction for three fixed values of R . We have also explored simulations with different values of n_{e0} , and found that, to reproduce the morphology of the observed Fermi bubbles, the required jet power increases with n_{e0} (i.e., with the densities of the hot halo gas). The observed gamma-ray surface brightness can in principle put a lower limit on the CR energy density within the bubbles, which may be used to constrain the properties of the hot halo gas. We plan to study this issue in a follow-up paper.

2.4. Numerical Setup and Jet Injection

Equations (1) – (4) are solved in (R, z) cylindrical coordinates using a 2D axisymmetric Eulerian code similar to ZEUS 2D (Stone & Norman 1992). In particular, our code follows the evolution of both hot gas and CRs, implementing their dynamical interaction, CR diffusion, and an energy equation for CRs. The CR diffusion is solved by using operator-splitting and a fully implicit Crank-Nicolson differencing method. While this differencing scheme is stable, we restrict each time step by the stability condition for explicitly differenced diffusion, as well as Courant conditions for numerical stability. The computational grid consists of 400 equally spaced zones in both coordinates out to 20 kpc plus additional 100 logarithmically-spaced zones out to 50 kpc. The central 20 kpc in each direction is resolved to 0.05 kpc. For both thermal and CR fluids, we adopt outflow boundary conditions at the outer boundary and reflective boundary conditions at the inner boundary.

The jet inflow is introduced with a constant speed v_{jet} along the z -axis (perpendicular to the Galactic plane) from the GC. During the active AGN phase $0 \leq t \leq t_{\text{jet}}$, the jet is initialized in a cylinder on the computational grid with radius R_{jet} and length z_{jet} beginning at the GC. All the physical variables in this cylinder are updated uniformly with the jet parameters at every time step during this phase. The jet contains both thermal gas and relativistic CRs, which are initialized inside the jet source cylinder and injected into the Galaxy at $z = z_{\text{jet}}$ with the jet speed having an initial opening angle of 0° . In the simulations presented in this paper, we take $z_{\text{jet}} = 0.5 \text{ kpc}$. This allows us to avoid modeling the complex jet evolution closer to the GC, which would require higher spatial resolution and involves uncertain multi-phase gas properties. We further assume that the jet has undergone

significant deceleration and transverse expansion within the jet source region ($0 \lesssim z \lesssim z_{\text{jet}}$), as seen in some extragalactic AGN jets (e.g., Laing et al. 2006). In our calculations, we thus investigate jets with $R_{\text{jet}}/z_{\text{jet}} \sim 0.2-1$ and $v_{\text{jet}}/c \sim 0.05-0.3$, where c is the speed of light. We stop the calculation at the current age of the Fermi bubbles $t = t_{\text{Fermi}}$, which is defined as the time when the produced CR bubble reaches the most distant boundary of the observed northern Fermi bubble along the jet axis. If the CR bubble does not reach this boundary within 3 Myr, we stop the calculation at $t = 3$ Myr.

The initial jet is described by six parameters: the thermal gas density ρ_j , the gas energy density e_j , the CR energy density e_{cr} , the jet velocity v_{jet} , the jet radius R_{jet} , and the jet duration t_{jet} . From ρ_j , one can derive the commonly-used jet density contrast between thermal gas inside the jet and the ambient hot gas: $\eta = \rho_j/\rho_{\text{amb}}$, where ρ_{amb} is the initial gas density at $(R, z) = (0, z_{\text{jet}})$. The jet power can be written as

$$P_{\text{jet}} = P_{\text{ke}} + P_{\text{cr}} + P_{\text{th}}, \quad (10)$$

where $P_{\text{ke}} = \rho_j v_{\text{jet}}^3 \pi R_{\text{jet}}^2 / 2$ is the jet kinetic power, $P_{\text{cr}} = e_{\text{cr}} v_{\text{jet}} \pi R_{\text{jet}}^2$ is the jet CR power, and $P_{\text{th}} = e_j v_{\text{jet}} \pi R_{\text{jet}}^2$ is the jet thermal power. The total energy injected by the jet can be written as $E_{\text{jet}} = P_{\text{jet}} t_{\text{jet}}$. Thermal and CR energy density are related to the gas and CR pressure respectively, thus both affecting the dynamical evolution of hot gas. Therefore e_j and e_{cr} are degenerate in our simulations: we can increase one while decreasing the other, reaching similar results (however, synchrotron and/or IC emissions from CRs can in principle break this degeneracy). In the simulations below, we take $e_j = e_{\text{amb}}$, where e_{amb} is the initial ambient gas energy density at $(R, z) = (0, z_{\text{jet}})$. In simulations that successfully produce Fermi bubbles as observed, we find that e_{cr} usually dominates over e_j . In other words, successful jets are usually over-pressured relative to the ambient hot gas at $z = z_{\text{jet}}$. As explained above, the jet simulations have a very large parameter space, and our 2D calculations permit us to run a large number (more than 100) simulations with different parameters within a reasonable amount of time. Here we present a few representative calculations particularly relevant to the Fermi bubbles, and list their jet parameters and derived jet properties in Table 1.

3. RESULTS

3.1. Forming Fermi Bubbles with AGN Jets

In this subsection, we present in detail one representative run (run A1), which approximately reproduces the morphology of the Fermi bubbles as observed in gamma-rays with the Fermi telescope. The main objective is to show that it is feasible to produce the observed Fermi bubbles from one single AGN jet activity from the GC. Other choices of jet parameters may produce similar results, so it is impossible to determine unique jet properties from the observed bubble morphology. Here we focus on some interesting features and problems in this representative run.

The edges of the bubbles are shown in Figure 18 of Su et al. (2010) in Galactic coordinates (l, b) . To compare our simulation results with observations, we derive the edges of the bubbles in our coordinates (R, z) using

the following coordinate conversion:

$$R = R_{\odot} |\tan(l)|, \quad (11)$$

$$z = \frac{R_{\odot}}{\cos(b)} \tan(b). \quad (12)$$

The resulting edge of the northern Fermi bubble is shown as the dotted region in each panel of Figure 2. The bubble is more elongated in (R, z) coordinates than in Galactic coordinates since $\partial z / \partial b \sim 1/\cos^2(b)$ increases significantly with b from $b = 0$ to $b \sim 50^\circ$. The line-of-sight projection may have a non-negligible effect on the coordinate conversion, since the bubble size is comparable to the distance between the Sun and the GC. The real bubble may be slightly smaller than the one shown in Figure 2. An accurate account for this effect requires three-dimensional structure of the bubbles, and is much more complex. We expect this effect to be small and neglect it in this paper.

The jet parameters for the fiducial run A1 are listed below: radius $R_{\text{jet}} = 0.4$ kpc, thermal electron number density $n_{\text{ej}} = 5.68 \times 10^{-4} \text{ cm}^{-3}$, gas energy density $e_j = 5.4 \times 10^{-11} \text{ erg cm}^{-3}$, CR energy density $e_{\text{cr}} = 1.0 \times 10^{-9} \text{ erg cm}^{-3}$, velocity $v_{\text{jet}} = 0.1c$, and duration $t_{\text{jet}} = 0.3$ Myr. The jet is light with a density contrast $\eta = 0.01$, which has been previously adopted in many jet simulations. Due to an additional CR component, the jet is over-pressured by a factor of ~ 10 with regard to the ambient hot gas at the jet base $z = z_{\text{jet}}$. Energetically the kinetic power in the jet dominates over the CR power by a factor of ~ 5 (see Table 1). The simulation is started at $t = 0$, and stopped at the current age of the Fermi bubbles $t = t_{\text{Fermi}} = 2.06$ Myr.

Figure 2 shows central slices of CR energy density (top panels) and electron number density (bottom panels) in logarithmic scale at $t = 1$ Myr (left panels), and $t = t_{\text{Fermi}} = 2.06$ Myr (right panels). As clearly seen, the jet produces a rapidly expanding CR bubble, which roughly matches the current north Fermi bubble (dotted circle) at $t = 2.06$ Myr. The CR transport is dominated by advection by the high velocity of thermal gas in the jet. The CR diffusivity in this run is low $\kappa = 3 \times 10^{27} \text{ cm}^2 \text{ s}^{-1}$, having a very small effect, which can also be seen by the sharp edge of the resulting CR bubble (see Section 3.2). The sharp edge is also an important feature of the observed Fermi bubbles. The lateral expansion of the bubble is mainly due to its high internal pressure (contributed by both CRs and shocked thermal gas) within the bubble and the rapidly decreasing ambient gas pressure with the galactocentric distance. The resulting CR bubble is much narrower if the initial jet has a smaller internal pressure. Due to the expansion, the gas density in the bubble is significantly lower than the ambient gas density, as clearly seen in the bottom panels of Figure 2. This explains why ROSAT X-ray observations show a ‘cavity’ of X-rays toward the center of the Fermi bubbles (similar to X-ray cavities often found in galaxy clusters).

The main difference between the simulated CR bubble and the observed Fermi bubbles is that the former suffers from Kelvin-Helmholtz instabilities at its surface (as clearly seen in Figure 2), while the real Fermi bubbles have smooth edges. Line-of-sight projection tends to

TABLE 1
 LIST OF SIMULATIONS

Run	κ ($\text{cm}^2 \text{s}^{-1}$)	R_{jet} (kpc)	t_{jet} (Myr)	η	e_{jcr}^a	v_{jet}	n_{ej}^b (10^{-4}cm^{-3})	t_{Fermi} (Myr)	P_{cr}^c	P_{ke}^c	P_{jet}^c	\dot{M}_{BH}^d M_{\odot}/yr	E_{jet}^e (10^{56}erg)
A1	3×10^{27}	0.4	0.3	0.01	1.0	0.1c	5.68	2.06	1.43	7.09	8.60	0.015	8.13
A-diff1	3×10^{28}	0.4	0.3	0.01	1.0	0.1c	5.68	1.94	1.43	7.09	8.60	0.015	8.13
A-diff2	3×10^{29}	0.4	0.3	0.01	1.0	0.1c	5.68	1.30	1.43	7.09	8.60	0.015	8.13
A-diff3	varied	0.4	0.3	0.01	1.0	0.1c	5.68	2.06	1.43	7.09	8.60	0.015	8.13
A2	3×10^{27}	0.4	0.3	0.02	1.5	0.1c	11.36	1.74	2.15	14.18	16.41	0.029	15.51
A3	3×10^{27}	0.4	0.2	0.01	3.0	0.2c	5.68	0.86	8.58	56.75	65.48	0.11	41.25
A4	3×10^{27}	0.2	0.3	0.05	6.0	0.1c	28.40	2.34	2.15	8.87	11.03	0.019	10.42
B1	3×10^{27}	0.4	0.3	0.0001	1.0	0.1c	0.057	-	1.43	0.07	1.58	0.0028	1.49
B2	3×10^{27}	0.4	0.3	0.5	1.0	0.05c	284	0.89	0.72	44.33	45.08	0.079	42.6

^aThe initial CR energy density in the jet base (in units of $10^{-9} \text{erg cm}^{-3}$).

^b n_{ej} is the initial thermal electron number density in the jet base: $n_{\text{ej}} = \rho_j / (\mu_e m_\mu)$.

^c P_{cr} , P_{ke} , and P_{jet} are, respectively, the jet CR, kinetic, and total powers (in units of $10^{43} \text{erg s}^{-1}$). $P_{\text{jet}} = P_{\text{ke}} + P_{\text{cr}} + P_{\text{th}}$, where the thermal jet power P_{th} is much smaller than P_{ke} and/or P_{cr} in our runs.

^d \dot{M}_{BH} is the corresponding accretion rate of the supermassive black hole at the GC, assuming a feedback efficiency of 10%: $\dot{M}_{\text{BH}} = P_{\text{jet}} / (0.1c^2)$.

^e $E_{\text{jet}} = P_{\text{jet}} t_{\text{jet}}$ is the energy injected by one jet during the AGN phase $0 \leq t \leq t_{\text{jet}}$. The total energy injected by both bipolar jets is $2E_{\text{jet}}$.

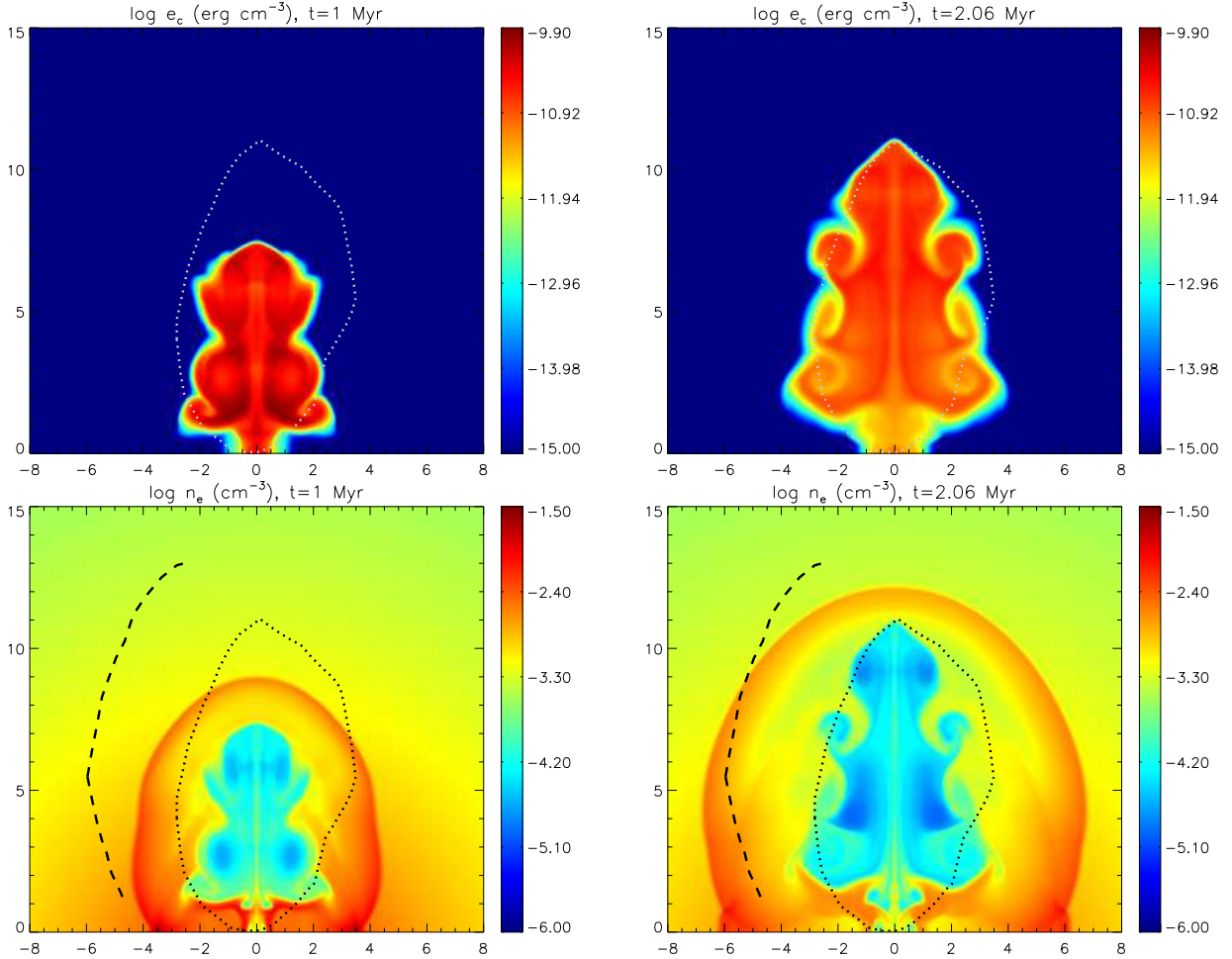


FIG. 2.— Central slices (16×15 kpc) of CR energy density (top panels) and electron number density (bottom panels) in logarithmic scale in run A1 at $t = 1$ Myr (left panels), and $t = t_{\text{Fermi}} = 2.06$ Myr (right panels). Horizontal and vertical axes refer to R and z respectively, labeled in kpc. The dotted region in each panel approximately encloses the observed north Fermi bubble. The propagation of the AGN jet, active for only $t_{\text{jet}} = 0.3$ Myr, produces a CR bubble at $t = 2.06$ Myr approximately matching the observed Fermi bubble. The dashed lines in bottom panels trace the outer edge of the *ROSAT* X-ray ‘northern arc’ feature, and is roughly spatially coincident with the jet-induced shock at $t = 2.06$ Myr.

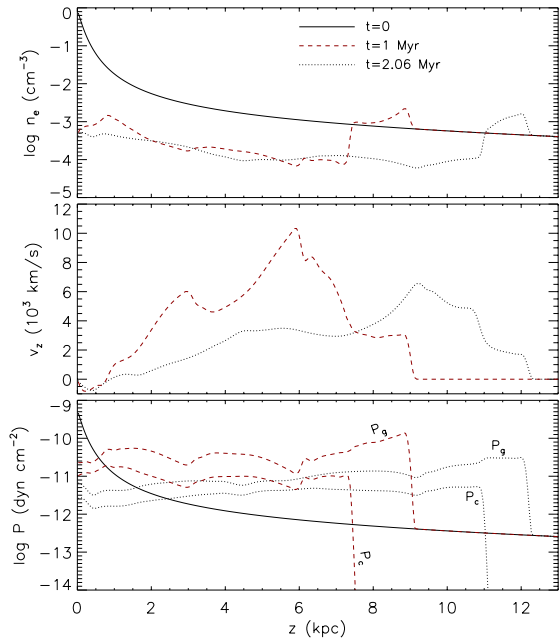


FIG. 3.— Variations of electron number density (top), the z -component gas velocity (middle), and pressures (bottom) along the jet axis for run A1 at $t = 1$ Myr (dashed) and $t = 2.06$ Myr (dotted). The initial gas density and pressure profiles along the z -axis at $t = 0$ are plotted as solid lines in the top and bottom panels, respectively.

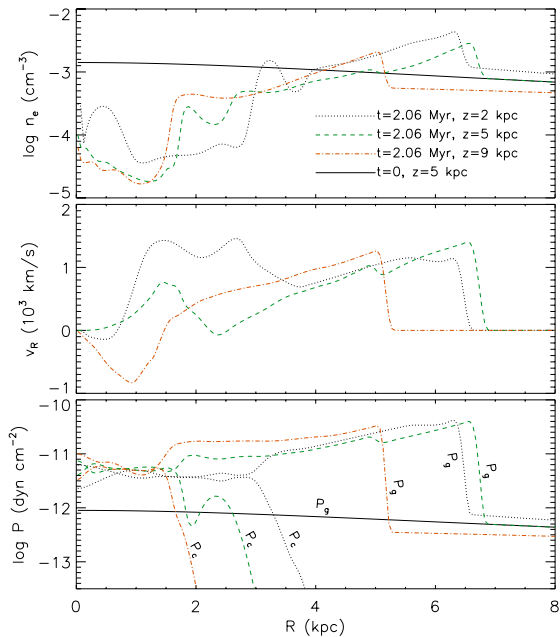


FIG. 4.— Variations of electron number density (top), the R -component gas velocity (middle), and pressures (bottom) along the R -direction (perpendicular to the jet axis) for run A1 at $t = 2.06$ Myr at $z = 2$ (dotted), 5 (dashed), and 9 kpc (dot-dashed). The initial gas density and pressure profiles along the R -direction at $z = 5$ kpc are plotted as solid lines in the top and bottom panels, respectively.

smooth the bubble edge when viewed in Galactic coordinates, but it is unable to completely remove surface irregularities created by Kelvin-Helmholtz instabilities. The same problem has been noticed in radio bubbles and X-ray cavities in galaxy clusters, where additional physics

is often invoked, e.g., viscosity (Reynolds et al. 2005) or tangled magnetic fields (Ruszkowski et al. 2007), to suppress Kelvin-Helmholtz instabilities. The situation may be similar for Fermi bubbles, where additional physics not included in our current calculations strongly suppresses the development of Kelvin-Helmholtz instabilities.

The bottom panels of Figure 2 show a strong shock produced by the jet activity. The shock propagates into the hot Galactic halo, and at $t = t_{\text{Fermi}}$ (i.e., the time when the bubbles are currently being observed), has a speed of ~ 2000 km/s (mach number $M \sim 9$) at the north shock front. The propagating shock can also be seen in Figure 3, which shows variations of electron number density, the z -component of the gas velocity v_z , and pressures along the jet axis at $t = 1$ Myr and $t = 2.06$ Myr. In directions perpendicular to the jet axis, the shock has a slightly smaller speed, reaching $R \sim 6$ kpc at $t = t_{\text{Fermi}}$, as seen in Figure 2. The shock front in the East direction is roughly spatially coincident with the outer edge of the *ROSAT* X-ray ‘northern arc’ feature (dashed line; Su et al. 2010). The shocked gas inside the shock front has higher densities ($n_e \sim 1 - 4 \times 10^{-3}$ cm $^{-3}$) and temperatures ($T \sim 3 - 7$ keV), thus naturally explaining the X-ray features enclosing both Fermi bubbles. At $t = t_{\text{Fermi}}$, the shock front in the East direction has a speed of ~ 1800 km/s. At a distance of $R_{\odot}/\cos(35^{\circ}) \approx 10.4$ kpc, the shock front (i.e., the outer edge of the X-ray feature) requires about 27 yrs to move an arcsecond, the approximate resolution of the *Chandra X-ray Telescope*.

The strong shock ($M \sim 8 - 9$) shown in Figures 2, 3 and 4 indicates that the Fermi bubbles are expanding explosively, only slightly decelerated by the small inertial resistance of the surrounding halo gas. The average total pressure inside our computed Fermi bubbles is about 50 - 100 times larger than that in the un-shocked ambient halo gas. This is very different compared to radio bubbles and X-ray cavities in galaxy clusters, where usually weak shocks with Mach number $M \sim 1 - 2$ are induced.

The internal structure of the CR bubble can be seen in Figure 4, which shows variations of electron number density, the R -component gas velocity v_R , and pressures along the R -direction (perpendicular to the jet axis) at $t = 2.06$ Myr at three different heights: $z = 2$ (dotted), 5 (dashed), and 9 kpc (dot-dashed). The bubble corresponds to regions with high CR pressure, and is surrounded by the outward-propagating shock represented by large jumps in n_e , v_R and P_g , which show the structure of the shock visible in Figure 2. The bubble has low gas densities $n_e \sim 1 - 8 \times 10^{-5}$ cm $^{-3}$, and is separated from the surrounding shocked gas through a contact discontinuity across which the total pressure is continuous. Within the bubble, the CR pressure is typically $\sim 3 - 6 \times 10^{-12}$ dyn cm $^{-2}$, which is comparable to the gas pressure, and slightly larger than the magnetic pressure of the $5 - 10$ μ G fields considered by Su et al. (2010) to explain the ‘WMAP haze’ observed at the base of the Fermi bubbles as synchrotron emission. This supports our neglect of the magnetic field in the bubble dynamics, which will likely not significantly change our results.

In run A1, the jet is energetically dominated by the kinetic energy, with the kinetic power $P_{\text{ke}} \sim 7.09 \times 10^{43}$ erg s $^{-1}$ and the CR power $P_{\text{Cr}} \sim 1.43 \times 10^{43}$ erg s $^{-1}$. The total jet power is $P_{\text{jet}} \sim 8.6 \times 10^{43}$ erg s $^{-1}$. The jet is

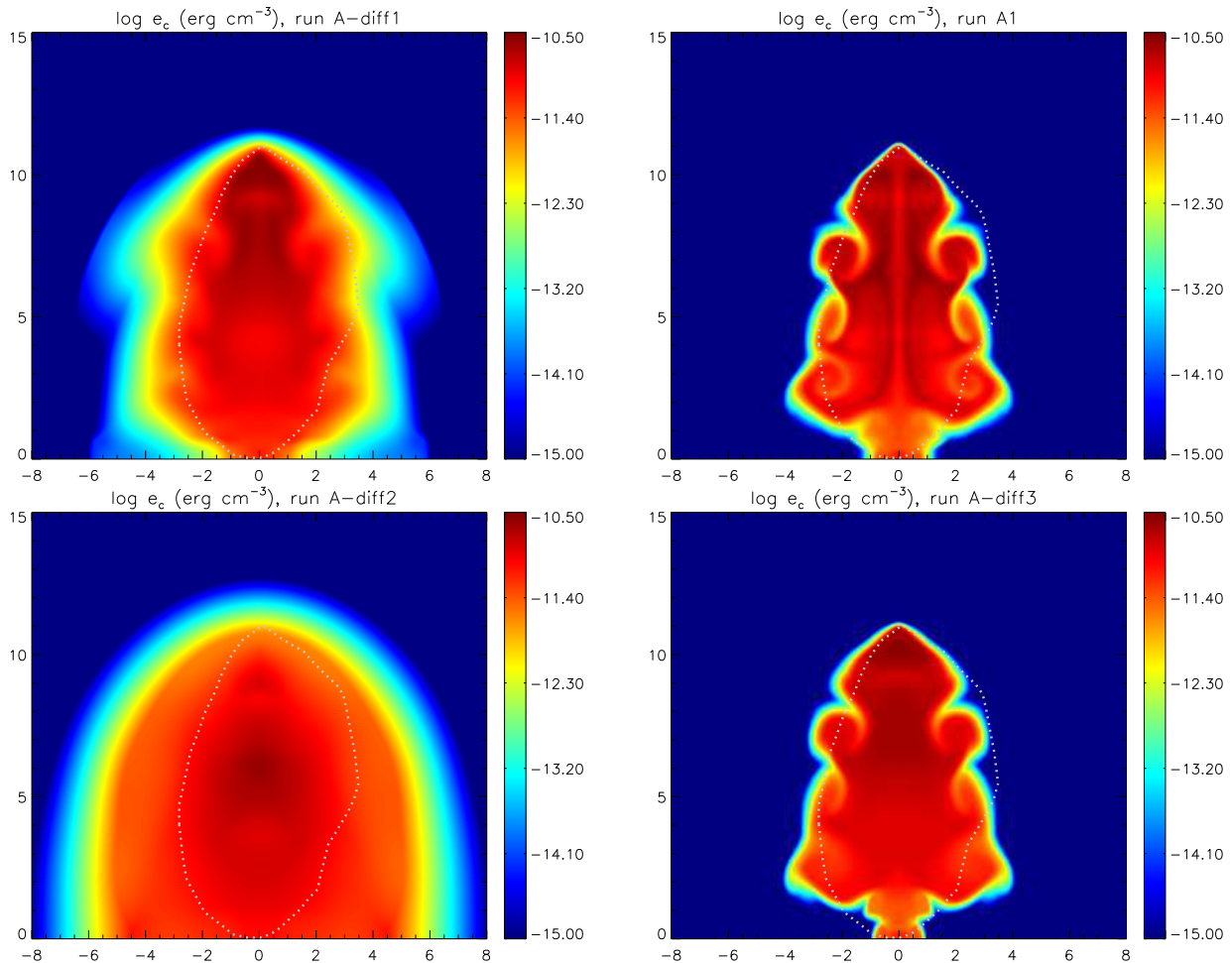


FIG. 5.— Central slices (16×15 kpc) of CR energy density in logarithmic scale in run A-diff1 (top-left), A1 (top-right), A-diff2 (bottom-left), and A-diff3 (bottom right) at $t = t_{\text{Fermi}}$ (details listed in Table 1 for each run). Horizontal and vertical axes refer to R and z respectively, labeled in kpc. The dotted region in each panel encloses the observed north Fermi bubble. In runs A-diff1 and A-diff2, CR diffusion significantly affects the bubble evolution, rendering bubble edges that are less sharp than those observed. Variable CR diffusion in run A-diff3 leads to a smoother CR energy density distribution inside the bubble, while still suppressing CR diffusion across the bubble surface and retaining sharp bubble edges as in run A1.

assumed to be produced by the supermassive black hole located at the GC. Taking a standard accretion efficiency of 10%, the black hole accretion rate can be determined $\dot{M}_{\text{BH}} = P_{\text{jet}}/(0.1c^2) = 1.5 \times 10^{-2} M_{\odot}/\text{yr}$. Assuming that the supermassive black hole has a mass of $M_{\text{BH}} \sim 4 \times 10^6 M_{\odot}$ (Ghez et al. 2008), the Eddington luminosity is $L_{\text{Edd}} \sim 5.5 \times 10^{44} \text{ erg s}^{-1}$, and the Eddington ratio for the AGN activity is $\epsilon = P_{\text{jet}}/L_{\text{Edd}} \sim 0.16$.

3.2. Suppression of CR Diffusion across the Bubble Surface

In our fiducial run A1, we choose a constant CR diffusion coefficient $\kappa = 3 \times 10^{27} \text{ cm}^2 \text{ s}^{-1}$, which is much lower than typical estimates of diffusivity in our Galaxy $\kappa \sim (3-5) \times 10^{28} \text{ cm}^2 \text{ s}^{-1}$. A low value for κ is specifically chosen to produce the CR bubble with sharp edge, which is one of the main features in the observed Fermi bubbles. When the diffusivity is not strongly suppressed, the edges of the resulting CR bubble are usually very broad, inconsistent with observations. To study the effect of CR diffusion on the bubble evolution, we perform three additional runs A-diff1, A-diff2, and A-diff3, which are all the same as run A1, but with different prescriptions for

the CR diffusivity κ .

In run A-diff1 and A-diff2, the CR diffusion coefficient is chosen to be $\kappa = 3 \times 10^{28}$, and $3 \times 10^{29} \text{ cm}^2 \text{ s}^{-1}$, respectively. In these cases, diffusion helps transport CRs, and thus the age of the CR bubble, $t_{\text{Fermi}} = 1.94, 1.30$ Myr respectively, is shorter than that in run A1. The 2D distribution of CR energy density at $t = t_{\text{Fermi}}$ in these runs is shown in left panels of Figure 5. When compared with run A1 (right-top panel), CR diffusion in runs A-diff1 and A-diff2 transports CRs to much large distances in the R direction, which is also clearly seen in Figure 6, which shows variations of CR pressure P_c along the R -direction at $t = t_{\text{Fermi}}$ at $z = 2$ (bottom), and 9 kpc (top) in runs A1, A-diff1, A-diff2, and A-diff3.

An important feature of the CR bubble produced in runs A-diff1 and A-diff2 is that the bubble edge is not sharp, as clearly seen in Figures 5 and 6. In contrast, the CR bubble in our fiducial run A1, where the CR diffusion coefficient is significantly suppressed, has sharp edges. Observations of Fermi bubbles indicate that the bubble edge is very sharp (Su et al. 2010), which, however, does not imply that the CR diffusion coefficient is strongly suppressed everywhere in the Galaxy. But it does mean that the CR diffusion across the bubble surface is signifi-

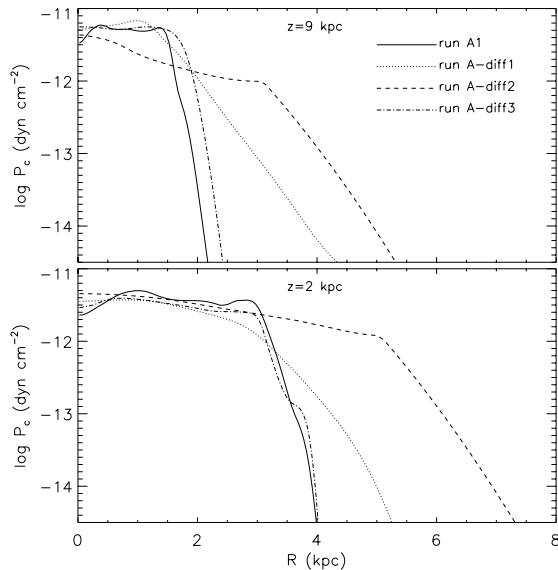


FIG. 6.— Variations of CR pressure P_c along the R -direction at $t = t_{\text{Fermi}}$ at $z = 2$ (bottom), and 9 kpc (top) in runs A1 (solid), A-diff1 (dotted), A-diff2 (dashed), and A-diff3 (dot-dashed). The edge of the CR bubble is not sharp in runs A-diff1 and A-diff2 because of CR diffusion across the bubble boundary.

cantly suppressed, which is the key to produce a CR bubble with sharp edges. CR diffusion is anisotropic, with diffusion across magnetic field lines strongly suppressed. It is likely that the magnetic field lines on the bubble surface are mainly tangential, since the gas surrounding the expanding CR bubble is significantly compressed. It is the tangential magnetic field that strongly suppresses the CR diffusion across the bubble surface, confining CRs within the CR bubble. It will be of great interest in the future to study this issue in detail using magnetohydrodynamic simulations with anisotropic CR diffusion.

As a first step, we try to mimic the suppression of CR diffusion across the bubble surface with our current simulation in run A-diff3. Since the CR bubble is associated with low gas density, we assume that the CR diffusivity in this run is related to the gas density:

$$\kappa = \begin{cases} 3 \times 10^{29} (n_{e0}/n_e) \text{ cm}^2 \text{ s}^{-1} & \text{when } n_e > n_{e0} \\ 3 \times 10^{29} \text{ cm}^2 \text{ s}^{-1} & \text{when } n_e \leq n_{e0}, \end{cases} \quad (13)$$

where $n_{e0} = 10^{-5} \text{ cm}^{-3}$. During the calculation of this run ($t \leq t_{\text{Fermi}}$), CR diffusion is significantly suppressed across the bubble surface ($\kappa \lesssim 10^{28} \text{ cm}^2 \text{ s}^{-1}$), but not suppressed within the CR bubble ($\kappa \sim 10^{28} - 10^{29} \text{ cm}^2 \text{ s}^{-1}$). At $t = t_{\text{Fermi}}$, the CR energy density distribution, shown in the bottom-right panel of Figure 5, is very similar to that in run A1 (top-right panel). The main difference is that the e_c distribution inside the bubble in run A-diff3 is much smoother than in run A1, which is obviously due to the stronger CR diffusion within the bubble in run A-diff3. The observed Fermi bubbles have approximately uniform surface brightness, which may imply that the CR diffusion is not suppressed inside the bubbles (i.e., only the diffusion across the bubble surface is suppressed). Future data from even longer-duration Fermi observations are needed to study the possible internal structure of the Fermi bubbles.

3.3. Constraints on the Jet Density

The jet simulation involves a large number of parameters, many of which are degenerate. It is thus impossible to accurately determine all jet properties from the morphology of the observed Fermi bubbles. Here we present results of a few additional essentially degenerate runs (A2, A3, and A4), all of which roughly produce the morphology of Fermi bubbles. The jet parameters and some results are summarized in Table 1. Comparing to run A1, the jet is more massive in run A2 ($\eta = 0.02$), faster in run A3 ($v_{\text{jet}} = 0.2c$), and narrower in run A4 ($R_{\text{jet}} = 0.2 \text{ kpc}$). The age of Fermi bubbles in these runs is $t_{\text{Fermi}} = 1.74, 0.86, 2.34 \text{ Myr}$ respectively. The 2D distribution of CR energy density at $t = t_{\text{Fermi}}$ in these runs is shown in Figure 7, where the electron number density distribution in run A2 is also shown in the bottom-left panel. In run A2, the shock fits even better with the outer edge of the X-ray feature (dashed line) than in run A1, strengthening the point that the *ROSAT* X-ray features surrounding the Fermi bubbles are produced by shocked gas associated with the jet activity. These four runs are representative of successful jet models, indicating that the Fermi bubbles are produced by a powerful AGN jet event which began about 1 - 2 Myr ago, and was active for a duration of $\sim 0.1 - 0.5 \text{ Myr}$, releasing a total energy of $\sim 1 - 8 \times 10^{57} \text{ erg}$. Here the total energy of the responsible AGN outburst depends on the densities of the confining halo gas, while its triggering time and duration do not. For a gaseous halo with fixed temperature, its initial density distribution can be scaled up or down by varying the central gas density n_{e0} . Equations 1 - 4 ensure that the evolution of the jet and resulting CR bubble is the same if the following three jet properties – density ρ_j and thermal energy density e_j , and CR energy density e_{jcr} , are scaled by the same factor as n_{e0} .

It is hard to accurately determine the jet properties, but it is possible to put some useful constraints, particularly on the jet density. When the jet is very light, e.g., $\eta = 0.0001$ as in run B1 (see Table 1 for other jet parameters), it quickly decelerates in the hot gas, and expands laterally in the R direction due to the high pressure within the bubble. The top panel of Figure 8 shows the CR energy density in logarithmic scale at $t = 3 \text{ Myr}$. As clearly seen, the jet only reaches $z \sim 6 \text{ kpc}$ at this time, and the resulting CR bubble is quasi-spherical, unlike the observed Fermi bubbles elongated in the radial direction. Very light jets tend to have strong backflows (i.e., with $v_z < 0$ inside the bubble at large R), which expand laterally, forming CR bubbles much ‘fatter’ than Fermi bubbles (see Guo & Mathews 2011). We have experimented with more runs with different jet densities, and find that the Fermi bubbles can be successfully reproduced only with jet densities $\eta \gtrsim 0.001$.

On the other hand, when the jet is very massive, e.g., $\eta = 0.5$ as in run B2 (see the bottom panel of Figure 8), it decelerates very slowly, producing very little backflow. In this case, most of the CRs are advected by the jet to the jet tip, not forming a ‘fat’, radially-elongated bubble as observed. We have run many simulations with high jet densities, and found the formed CR bubbles are usually much thinner than the observed Fermi bubbles. Acceptable runs typically have the jet density contrast $\eta \lesssim 0.1$.

AGN jets efficiently transport CRs from the GC to the Galactic halo. Additionally the jets can produce or reac-

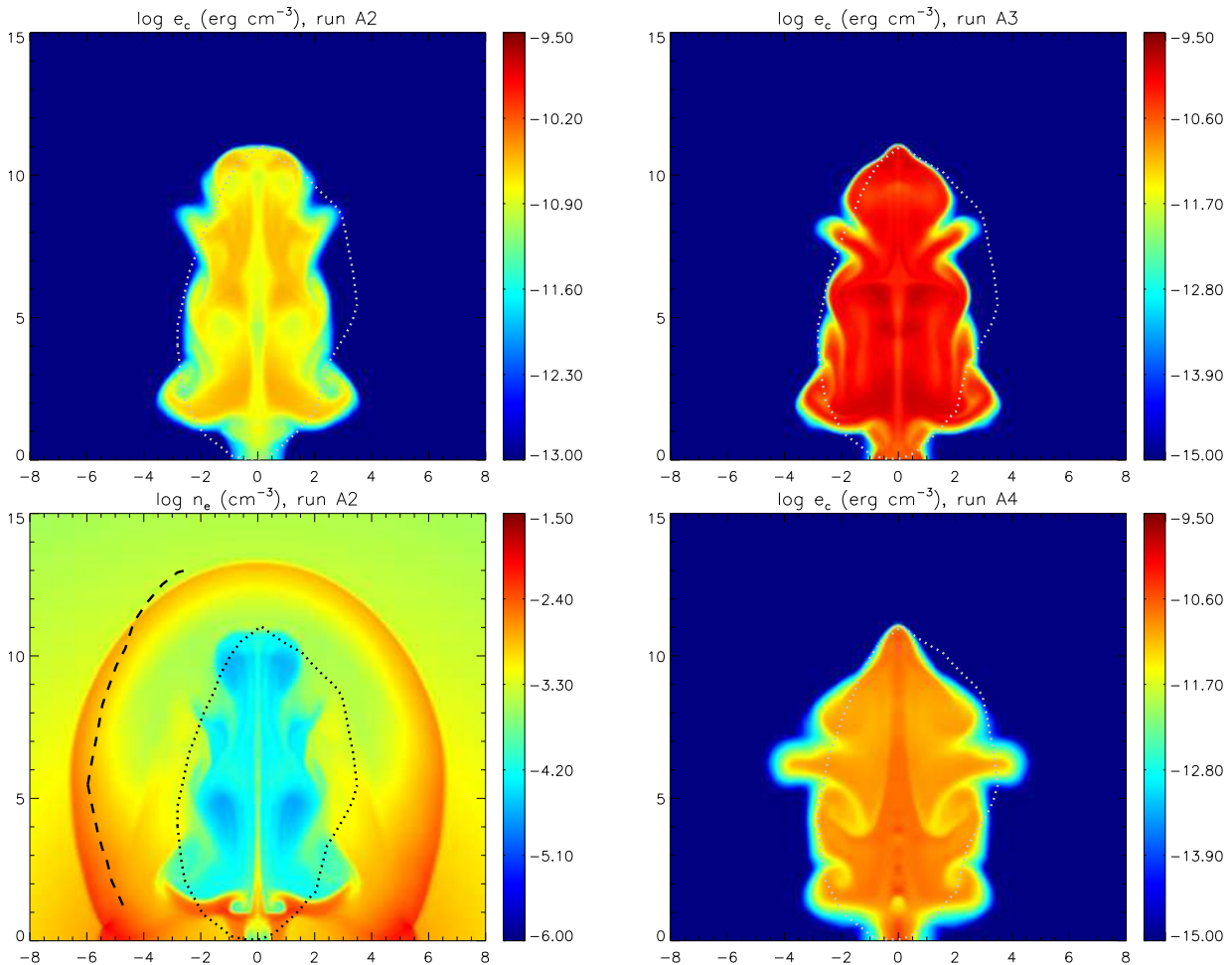


FIG. 7.— Central slices (16×15 kpc) of $\log(e_c)$ in run A2 (top-left), A3 (top-right), A4 (bottom-right), and $\log(n_e)$ in run A2 (bottom left) at $t = t_{\text{Fermi}}$ (details listed in Table 1 for each run), when the simulated CR bubble reaches the most distant edge of the observed north Fermi bubble. Horizontal and vertical axes refer to R and z respectively, labeled in kpc. The dotted region in each panel encloses the observed north Fermi bubble. The dashed lines in the bottom-left panel trace the outer edge of the *ROSAT* X-ray ‘northern arc’ feature. Run A1 and these additional runs have different jet parameters, but all produce CR bubbles approximately matching the observed Fermi bubbles.

celerate CRs in the strong shock at the jet tip (hot spot) which we have not considered here. The morphology and evolution of the resulting CR bubble significantly depend on many jet properties, but the jet density contrast is particularly important. From the morphology of the Fermi bubbles, we can approximately constrain the jet density contrast: $0.001 \lesssim \eta \lesssim 0.1$, which corresponds to $6 \times 10^{-5} \text{ cm}^{-3} \lesssim n_{\text{ej}} \lesssim 6 \times 10^{-3} \text{ cm}^{-3}$ for our adopted model for the Galactic thermal atmosphere. The constraint on the jet density contrast η is quite robust, not depending on the value of n_{e0} , the density normalization of the ambient halo gas.

4. SUMMARY AND IMPLICATION

The detection of Fermi bubbles in the Galaxy is one of the most important and striking findings during the first two years’ observations of the *Fermi Gamma-ray Space Telescope*. The bubbles are symmetric about the GC, with one above and the other below the Galactic plane. The surface brightness in γ -ray emission from the bubbles is quite uniform with sharp edges at the bubble boundaries. These observed properties make it very difficult to explain the bubbles in many of the standard ways, for example by supernova shocks in the Galactic

plane or by dark matter annihilations.

The unique location and morphology of the bubbles suggest that they were most likely created by some large episode of energy injection in the GC. Gamma rays from the bubbles can be produced by IC emission of CRe at tens of GeV or even higher energies, whose cooling times are very short, less than a few Myr. Yet *Fermi* observations show that the gamma ray spectrum from the bubbles is very hard with little evidence of IC cooling, indicating that the bubbles must be formed rapidly, and Galactic winds are probably too slow to transport CRe from the GC. In analogy with extragalactic double radio sources and X-ray cavities, we investigate in this paper if AGN jets from the GC can create the Fermi bubbles with the observed location and morphology.

In our model, a pair of bipolar jets were released from the GC along the symmetric axis perpendicular to the Galactic plane. We model the jet evolution using a series of 2D axisymmetric hydrodynamical simulations, which additionally follow the evolution of CRe and their dynamical interactions with thermal gas (see Section 2.2). Thus we model CR advection self-consistently. Our calculations also take into account CR diffusion.

We show that the observed Fermi bubbles can be re-

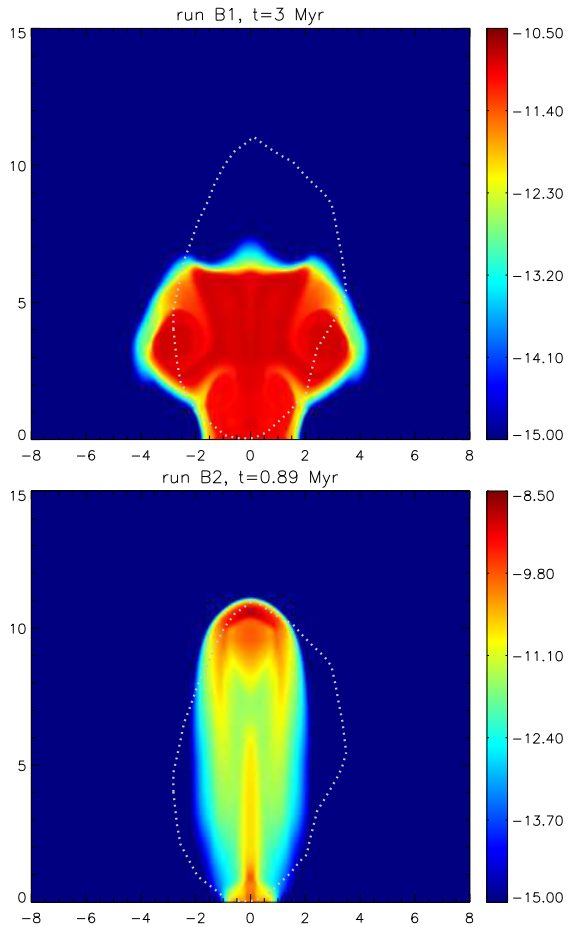


FIG. 8.— Central slices (16×15 kpc) of CR energy density in logarithmic scale in run B1 at $t = 3$ Myr (top) and B2 (bottom) at $t = t_{\text{Fermi}}$. Horizontal and vertical axes refer to R and z respectively, labeled in kpc. The dotted region in each panel encloses the observed north Fermi bubble. Very light jets in run B1 ($\eta = 0.0001$) decelerate rapidly in the halo gas, forming quasi-spherical CR bubbles unlike the radially elongated Fermi bubbles observed. On the other hand, the massive jets in run B2 ($\eta = 0.5$) transport most CRs just along the z axis, not forming the ‘fat’ bubbles observed.

produced by a recent AGN jet activity about 1 - 2 Myr ago, which was active for a duration of $\sim 0.1 - 0.5$ Myr, releasing a typical total energy of $\sim 1 - 8 \times 10^{57}$ erg. Containing both thermal gas and CRs, the two-fluid jet quickly advects CRs to high latitude. The jet is energetically dominated by the kinetic energy, and over-pressured with CR pressure which induces lateral expansion, creating a fat CR bubble as observed. In our fiducial run A1, the jet has a power of $P_{\text{jet}} \sim 8.6 \times 10^{43}$ erg s^{-1} , corresponding to an accretion rate of $\dot{M}_{\text{BH}} \sim 0.015 M_{\odot}/\text{yr}$ for the central black hole and an Eddington ratio of $\epsilon \sim 0.16$. The jet activity also induces a strong oval-shaped shock (currently Mach number $M \sim 8 - 9$), which heats and compresses the ambient gas in the Galactic halo, successfully explaining the *ROSAT* X-ray features surrounding the Fermi bubbles.

Because of the degeneracy of successful bubble models with different jet parameters, it is difficult or impossible to determine unique jet parameters directly from the bubble location and morphology. However, we can put some useful constraints on them, particularly on the jet density contrast relative to the ambient hot gas at the jet base. Very low density, ultra-light jets decelerate quickly

and usually form quasi-spherical bubbles unlike the observed Fermi bubbles which are radially elongated. In contrast, heavy, massive jets decelerate very slowly, advecting most CRs to the tip of the jet with too little lateral expansion. Successful jets are moderately light, having typical density contrasts $0.001 \lesssim \eta \lesssim 0.1$ (i.e., $6 \times 10^{-5} \text{ cm}^{-3} \lesssim n_{\text{ej}} \lesssim 6 \times 10^{-3} \text{ cm}^{-3}$ for our adopted model for the Galactic thermal atmosphere).

We also show that to produce sharp edges of the bubbles, CR diffusion across the bubble surface must be strongly suppressed. CR advection is responsible for the spatial expansion of the Fermi bubbles, which compresses thermal gas near the bubble surface, aligning the local magnetic fields to be tangential to the bubble boundary. CR diffusion is probably anisotropic, with cross-field diffusion strongly suppressed. However, it is likely that CR diffusion deeper inside the bubbles is not suppressed and it tends to remove small CR structures, resulting in more uniform CR distribution and γ -ray emission within the bubbles as suggested by Fermi observations.

Fermi bubbles provide strong evidence for a recent powerful AGN jet activity in the Milky Way. Extragalactic jets have been detected in many distant galaxies, such as the famous jet in M87 (Junor et al. 1999; Kovalev et al. 2007). Numerous bipolar radio bubbles and X-ray cavities have also been observed, clearly associated with the central stellar bulges of massive galaxies. These non-thermal regions are almost certainly produced by AGN jets, which are often not detectable because of the short time when they are active (McNamara & Nulsen 2007). Multi-wavelength studies show that AGN jet activity deposits large amounts of mechanical and CR energy into the host environments, significantly affecting the evolution of gas and host galaxies. But in our Galaxy there is little evidence for an active AGN jet today. The detection of Fermi bubbles as the remnant of a recent powerful AGN jet event is thus of dramatic astronomical importance, suggesting that AGN jet activity may also happen regularly in our Galaxy. Powerful AGN jets have a strong impact on the multi-phase gas in the Galactic bulge and halo. In the bulge, AGN jets may heat and expel thermal gas, efficiently shutting off star formation, black hole accretion and regulating the co-evolution of the massive black hole and the stellar bulge. Many interesting questions remain unanswered: Which gas components (hot, atomic or molecular) are significantly impacted by AGN jets and bubbles? What triggers the AGN activity? What is the jet duty cycle? The answers to these questions may significantly advance our understanding on the origin of the remarkably tight correlations between central black holes and their host bulges.

Furthermore, AGN activity from the GC may contribute significantly to, or dominate, the CR population in the Galactic halo. Suppose for example that new pairs of Fermi bubbles with total CR energy 2.7×10^{56} ergs (twice that of the single bubble in run A1) are produced every 30 Myr (AGN duty cycle $\sim 1\%$). This would supply CR energy to the Galactic halo at a rate 2.86×10^{41} ergs s^{-1} . By comparison, if one supernova of energy 10^{51} ergs occurs in the Galaxy every 50 years and 10% of that energy is converted to CRs, the total CR power generated, 0.6×10^{41} ergs s^{-1} , is considerably less than

the estimated rate from AGN activity. Nevertheless, CRs from previous generations of Fermi bubbles may not contribute significantly to the locally observed CR energy density – this would require that CRs return to the solar vicinity by relatively slow diffusion in the halo before buoyancy and kinetic energy of the moving bubbles carry

them entirely out of the Galactic halo.

FG would like to thank Fabrizio Brighenti, Matthew McQuinn, S. Peng Oh and Aristotle Socrates for helpful discussions.

REFERENCES

- Breitschwerdt, D., McKenzie, J. F., & Voelk, H. J. 1991, *A&A*, 245, 79
- Dobler, G., & Finkbeiner, D. P. 2008, *ApJ*, 680, 1222
- Dobler, G., Finkbeiner, D. P., Cholis, I., Slatyer, T., & Weiner, N. 2010, *ApJ*, 717, 825
- Ferrarese, L., & Merritt, D. 2000, *ApJ*, 539, L9
- Finkbeiner, D. P. 2004, *ApJ*, 614, 186
- Gebhardt, K., et al. 2000, *ApJ*, 539, L13
- Ghez, A. M., et al. 2008, *ApJ*, 689, 1044
- Guo, F., & Mathews, W. G. 2010a, *ApJ*, 712, 1311
- . 2010b, *ApJ*, 717, 937
- . 2011, *ApJ*, 728, 121
- Guo, F., & Oh, S. P. 2008, *MNRAS*, 384, 251
- Helmi, A., & White, S. D. M. 2001, *MNRAS*, 323, 529
- Junor, W., Biretta, J. A., & Livio, M. 1999, *Nature*, 401, 891
- Kovalev, Y. Y., Lister, M. L., Homan, D. C., & Kellermann, K. I. 2007, *ApJ*, 668, L27
- Kulsrud, R. M. 2005, *Plasma physics for astrophysics* (Princeton University Press, Princeton, NJ)
- Laing, R. A., Canvin, J. R., Bridle, A. H., & Hardcastle, M. J. 2006, *MNRAS*, 372, 510
- Magorrian, J., et al. 1998, *AJ*, 115, 2285
- Mathews, W. G. 2009, *ApJ*, 695, L49
- Mathews, W. G., & Brighenti, F. 2008a, *ApJ*, 676, 880
- . 2008b, *ApJ*, 685, 128
- Mathews, W. G., & Guo, F. 2010, *ApJ*, 725, 1440
- McNamara, B. R., & Nulsen, P. E. J. 2007, *ARA&A*, 45, 117
- Reynolds, C. S., McKernan, B., Fabian, A. C., Stone, J. M., & Vernaleo, J. C. 2005, *MNRAS*, 357, 242
- Ruszkowski, M., Enßlin, T. A., Brügggen, M., Heinz, S., & Pfrommer, C. 2007, *MNRAS*, 378, 662
- Skilling, J. 1971, *ApJ*, 170, 265
- Stone, J. M., & Norman, M. L. 1992, *ApJS*, 80, 753
- Strong, A. W., & Moskalenko, I. V. 1998, *ApJ*, 509, 212
- Strong, A. W., Moskalenko, I. V., & Ptuskin, V. S. 2007, *Annual Review of Nuclear and Particle Science*, 57, 285
- Su, M., Slatyer, T. R., & Finkbeiner, D. P. 2010, *ApJ*, 724, 1044
- Wolfire, M. G., McKee, C. F., Hollenbach, D., & Tielens, A. G. G. M. 1995, *ApJ*, 453, 673
- Yao, Y., & Wang, Q. D. 2005, *ApJ*, 624, 751